

Cite this: *Nanoscale*, 2021, 13, 9766

## Enhancing multiphoton upconversion emissions through confined energy migration in lanthanide-doped Cs<sub>2</sub>NaYF<sub>6</sub> nanoplatelets†

Chang Zhou,<sup>a,b</sup> Datao Tu,<sup>a,b,c</sup> Siyuan Han,<sup>a</sup> Peng Zhang,<sup>a,b</sup> Luping Wang,<sup>a</sup> Shaohua Yu,<sup>a</sup> Jin Xu,<sup>a,c</sup> Renfu Li<sup>a,c</sup> and Xueyuan Chen<sup>a,b,c</sup>

Lanthanide (Ln<sup>3+</sup>)-doped upconversion (UC) nanocrystals have drawn tremendous attention because of their intriguing optical properties. Currently, it is highly desired but remains challenging to achieve efficient multiphoton UC emissions. Herein, we report the controlled synthesis of a new class of UC nanocrystals based on Cs<sub>2</sub>NaYF<sub>6</sub>:Yb/Tm nanoplatelets (NPs), which can effectively convert the 980 nm light to five-photon and four-photon UC emissions of Tm<sup>3+</sup> without the fabrication of a complicated core/multishell structure required in traditional nanocrystals. Particularly, the as-prepared Cs<sub>2</sub>NaYF<sub>6</sub>:Yb/Tm NPs exhibit a maximal UV-to-NIR emission intensity ratio of 1.2, which is the highest among Tm<sup>3+</sup>-doped core-only UC nanocrystals. We reveal that the enhanced multiphoton UC emissions may benefit from the confined energy migration of Ln<sup>3+</sup> dopants in the unique two-dimensional-like structure of Cs<sub>2</sub>NaYF<sub>6</sub> NPs. As such, intense red and green UC emissions of Eu<sup>3+</sup> and Tb<sup>3+</sup> can further be generated via the cascade sensitization of Tm<sup>3+</sup> and Gd<sup>3+</sup> in Cs<sub>2</sub>NaYF<sub>6</sub>:Yb/Tm/Gd/Eu and Cs<sub>2</sub>NaYF<sub>6</sub>:Yb/Tm/Gd/Tb NPs, respectively. These results validate the superiority of Cs<sub>2</sub>NaYF<sub>6</sub> for the future design of efficient UC nanocrystals towards versatile applications.

Received 19th March 2021  
Accepted 29th April 2021

DOI: 10.1039/d1nr01745d

rsc.li/nanoscale

## Introduction

Lanthanide (Ln<sup>3+</sup>)-doped upconversion (UC) nanocrystals can convert low-energy excitation to high-energy emission, which makes them attractive for applications in photocatalysis, anti-counterfeiting and biosensing.<sup>1–8</sup> Based on the unique ladder-like 4f energy configurations of Ln<sup>3+</sup> ions, UC emission from high energy levels is generated through successive absorption of low-energy photons with sensitizer ions (*e.g.*, Yb<sup>3+</sup>, Nd<sup>3+</sup>) and transfer of the energy to activator ions (*e.g.*, Er<sup>3+</sup>, Tm<sup>3+</sup>, Ho<sup>3+</sup>).<sup>9–14</sup> Theoretically, elevating the concentration of Ln<sup>3+</sup> dopants may improve the energy transfer efficiency and enhance the UC luminescence (UCL).<sup>15,16</sup> Unfortunately, a high concentration of dopants may cause concentration quenching of UCL due to the deleterious energy migration or

cross-relaxation processes between the neighboring Ln<sup>3+</sup> ions.<sup>17,18</sup> Moreover, the long-distance migration of excitation energy via highly concentrated Ln<sup>3+</sup> dopants to lattice/surface defects may severely deteriorate the multiphoton UC emission in the ultraviolet (UV) spectral region.<sup>19</sup>

Hitherto, substantial efforts have been made to overcome such obstacles and to enhance the multiphoton UV emission in Ln<sup>3+</sup>-doped UC nanocrystals.<sup>20–22</sup> Typically, a core/multishell structure has to be constructed to suppress the energy migration in traditional nanocrystals. For example, Zhou *et al.* designed NaYF<sub>4</sub>:Er@NaYbF<sub>4</sub>@NaYF<sub>4</sub> core/shell/shell nanocrystals to alleviate the energy back-transfer from Er<sup>3+</sup> to Yb<sup>3+</sup>, which promoted the three-photon UC emission of Er<sup>3+</sup>.<sup>23</sup> Chen *et al.* synthesized NaYF<sub>4</sub>@NaYbF<sub>4</sub>:Tm@NaYF<sub>4</sub> core/shell/shell nanocrystals, where efficient five-photon UCL of Tm<sup>3+</sup> was realized without suffering from concentration quenching of Yb<sup>3+</sup>.<sup>24</sup> To circumvent the complicated synthesis procedures of core/multishell nanocrystals, it is of utmost importance to explore special host lattices to confine energy migration between Ln<sup>3+</sup> dopants for producing intense multiphoton UC emissions.<sup>25,26</sup>

Cs<sub>2</sub>NaYF<sub>6</sub>, a face-centered cubic crystal with the space-group symmetry of *Fm*3*m*, has been reported as an excellent laser or scintillation host.<sup>27,28</sup> In the Cs<sub>2</sub>NaYF<sub>6</sub> crystal, Na<sup>+</sup> and Y<sup>3+</sup> ions are surrounded by six halogen ions that form an

<sup>a</sup>CAS Key Laboratory of Design and Assembly of Functional Nanostructures, Fujian Key Laboratory of Nanomaterials, and State Key Laboratory of Structural Chemistry, Fujian Institute of Research on the Structure of Matter, Chinese Academy of Sciences, Fuzhou, Fujian 350002, China. E-mail: dttu@fjirsm.ac.cn, xchen@fjirsm.ac.cn

<sup>b</sup>College of Chemistry, Fuzhou University, Fuzhou, Fujian 350108, China

<sup>c</sup>Fujian Science & Technology Innovation Laboratory for Optoelectronic Information of China, Fuzhou, Fujian 350108, China

†Electronic supplementary information (ESI) available. See DOI: 10.1039/d1nr01745d

octahedron. Particularly, the unit cell parameters  $a = b = c = 9.08 \text{ \AA}$  are much larger than those of widely reported  $\alpha\text{-NaYF}_4$  with the same space-group symmetry (unit cell parameters  $a = b = c = 5.47 \text{ \AA}$ ). As such, the energy migration between  $\text{Ln}^{3+}$  dopants is expected to be effectively confined.<sup>29,30</sup> So far, all the previous research studies of  $\text{Ln}^{3+}$ -doped  $\text{Cs}_2\text{NaYF}_6$  have been carried out *via* hydrothermal and solid-state reaction methods, which resulted in bulk materials.<sup>31,32</sup> Nowadays, it remains a great challenge to synthesize monodisperse  $\text{Ln}^{3+}$ -doped  $\text{Cs}_2\text{NaYF}_6$  nanocrystals, whose UCL properties and the related UC mechanism deserve to be investigated.

Herein, we propose a facile strategy for the controlled synthesis of  $\text{Ln}^{3+}$ -doped  $\text{Cs}_2\text{NaYF}_6$  nanoplatelets (NPs). Upon excitation at 980 nm, an integrated UV-to-NIR emission intensity ratio of up to 1.2 can be achieved based on the as-prepared  $\text{Cs}_2\text{NaYF}_6:\text{Yb}/\text{Tm}$  NPs, which is  $\sim 40$  times higher than that of  $\alpha\text{-NaYF}_4:\text{Yb}/\text{Tm}$  counterparts. By means of structural analysis, the enhanced multiphoton UCL mechanism is attributed to the inhibition of the energy migration between  $\text{Ln}^{3+}$  dopants in  $\text{Cs}_2\text{NaYF}_6$ . Furthermore, we demonstrate that intense UC emissions of  $\text{Eu}^{3+}$  and  $\text{Tb}^{3+}$  can be generated *via* the sensitization of  $\text{Tm}^{3+}$  and  $\text{Gd}^{3+}$  in  $\text{Cs}_2\text{NaYF}_6:\text{Yb}/\text{Tm}/\text{Gd}/\text{Eu}$  and  $\text{Cs}_2\text{NaYF}_6:\text{Yb}/\text{Tm}/\text{Gd}/\text{Tb}$  NPs, respectively (Scheme 1).

## Results and discussion

$\text{Cs}_2\text{NaYF}_6:\text{Yb}/\text{Tm}$  NPs were synthesized *via* a facile high-temperature co-precipitation method, where  $\text{CsF}$  reacted with metal precursors in the mixed solvents containing oleic acid (OA), oleylamine (OAm) and octadecene (ODE) (Fig. 1a). X-ray diffraction (XRD) patterns show that all the diffraction peaks of the as-prepared NPs match well with the cubic  $\text{Cs}_2\text{NaYF}_6$  (JCPDS no. 20-1214). Compared with those of the bulk counterparts synthesized *via* the solid-state reaction method (Fig. S1†), the XRD peaks of these NPs are broadened, indicating the smaller size of the as-prepared NPs (Fig. 1b). The growth rate of the NPs can be controlled with the reaction solvent because the

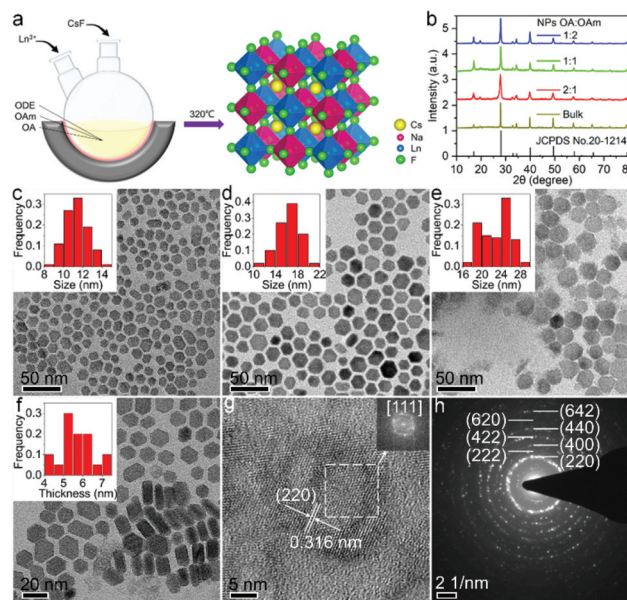
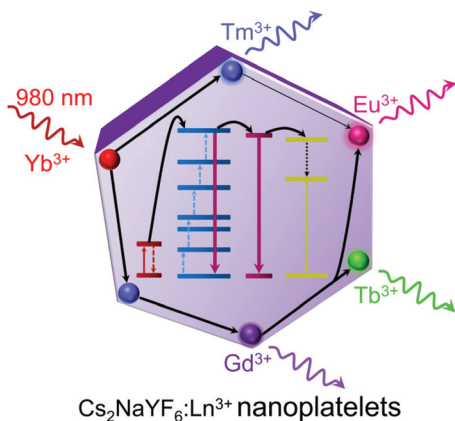


**Fig. 1** (a) Schematic illustration of the synthesis of  $\text{Cs}_2\text{NaYF}_6:\text{Yb}/\text{Tm}$  NPs. (b) XRD patterns of  $\text{Cs}_2\text{NaYF}_6:\text{Yb}/\text{Tm}$  NPs and bulk materials. (c–e) Bright-field TEM images of  $\text{Cs}_2\text{NaYF}_6:\text{Yb}/\text{Tm}$  NPs synthesized with an OA/OAm ratio of 2 : 1, 1 : 1, and 1 : 2, respectively. Insets: a size distribution histogram by randomly calculating 100 particles in the TEM images. (f) Bright-field TEM images of  $\text{Cs}_2\text{NaYF}_6:\text{Yb}/\text{Tm}$  NPs synthesized with an OA/OAm ratio of 2 : 1. The inset shows the thickness distribution histogram of the as-prepared NPs. (g) HRTEM and (h) SEAD of  $\text{Cs}_2\text{NaYF}_6:\text{Yb}/\text{Tm}$  NPs.

ion diffusion is faster at a lower OA/OAm ratio.<sup>33</sup> As a result, the size of NPs can be tuned by adjusting the OA/OAm ratio. When the OA/OAm ratio decreased from 2 : 1, 1 : 1 to 1 : 2, the average size increased from  $11.4 \pm 1.1 \text{ nm}$ ,  $16.4 \pm 1.9 \text{ nm}$  to  $22.9 \pm 2.9 \text{ nm}$  (Fig. 1c–e). The thickness of the  $\text{Cs}_2\text{NaYF}_6:\text{Yb}/\text{Tm}$  NPs was determined to be  $5.7 \pm 0.8 \text{ nm}$  (Fig. 1f). The high-resolution transmission electron microscopy (HRTEM) image of  $\text{Cs}_2\text{NaYF}_6$  NPs shows clear lattice fringes (Fig. 1g). The fast Fourier transform (FFT) image of the NPs from the HRTEM image indicates that there are six nearest scattering points around each white scattering point, and the distance between them is 0.316 nm, verifying that the dominant arrangement of the synthesized  $\text{Ln}^{3+}$  doped  $\text{Cs}_2\text{NaYF}_6$  NPs is the [111] orientation.<sup>34</sup> The selected-area electron diffraction (SAED) pattern of these NPs displays intense diffraction rings of cubic  $\text{Cs}_2\text{NaYF}_6$  (Fig. 1h), confirming the pure phase and high crystallinity of the obtained NPs. In addition, the energy-dispersive X-ray (EDX) spectrum confirms the successful doping of  $\text{Yb}^{3+}$  and  $\text{Tm}^{3+}$  in  $\text{Cs}_2\text{NaYF}_6$  NPs (Fig. S2†).

To examine the effect of  $\text{Ln}^{3+}$  dopants on UC emission, we synthesized a series of  $\text{Cs}_2\text{NaYF}_6:\text{Yb}/\text{Tm}$  NPs with different  $\text{Tm}^{3+}$  and  $\text{Yb}^{3+}$  concentrations. The optimal  $\text{Tm}^{3+}$  concentration was 1 mol%, which resulted in the maximal UCL emission upon excitation with a 980 nm laser (Fig. S3†). For  $\text{Cs}_2\text{NaYF}_6:x \text{ mol\% Yb}$ , 1 mol%  $\text{Tm}$  NPs with different  $\text{Yb}^{3+}$  concentrations (Fig. S4†), their UCL spectra consist of character-



**Scheme 1** Schematic illustration of  $\text{Cs}_2\text{NaYF}_6:\text{Ln}^{3+}$  NPs with highly efficient multiphoton UC emission upon 980 nm excitation.

istic sharp emission peaks which can be assigned to the five-photon  $^1I_6 \rightarrow ^3H_6$  and  $^3F_4$  (290 and 348 nm), four-photon  $^1D_2 \rightarrow ^3H_6$  and  $^3F_4$  (362 and 450 nm), three-photon  $^1G_4 \rightarrow ^3H_6$  and  $^3F_4$  (478 and 649 nm) and two-photon  $^3H_4 \rightarrow ^3H_6$  (803 nm) transitions of  $Tm^{3+}$  (Fig. 2a). Interestingly, the five-photon and four-photon UCL emissions of  $Cs_2NaYF_6:Yb/Tm$  NPs in the UV region were observed to be strikingly strong. With the  $Yb^{3+}$  concentration of 49 mol%, a maximum integrated UV-to-NIR emission intensity ratio can be achieved (Fig. 2b).

We then compared the UCL spectra of  $Cs_2NaYF_6:Yb/Tm$  NPs and bulk materials with that of typical  $Tm^{3+}$  doped fluoride nanocrystals like  $\alpha-NaYF_4$  (Fig. 2c). Bright blue UCL can be observed for these samples upon 980 nm excitation at a power density of  $150 \text{ W cm}^{-2}$ . The absolute upconversion quantum yields for the visible and NIR regions (400–850 nm) of  $Cs_2NaYF_6:Yb/Tm$  NPs and bulk have been determined to be  $0.10 \pm 0.02\%$  and  $1.27 \pm 0.10\%$ , respectively, which are higher than that of  $\alpha-NaYF_4:Yb/Tm$  nanocrystals ( $0.05 \pm 0.02\%$ ). Moreover, the five-photon and four-photon UCL emissions of  $Cs_2NaYF_6:Yb/Tm$  NPs in the UV region were observed to be much stronger than those of  $Tm^{3+}$  doped  $\alpha-NaYF_4$  nanocrystals

(Fig. S5†). The integrated UV-to-NIR emission intensity ratio of these samples increased with an increase in the excitation power density. With a power density of  $150 \text{ W cm}^{-2}$ , the UV-to-NIR ratios for  $Cs_2NaYF_6:49 \text{ mol\%Yb, 1 mol\%Tm}$  NPs and bulk materials were calculated to be 1.20 and 0.51, respectively, which are  $\sim 40$  and  $\sim 17$  times higher than that of  $\alpha-NaYF_4:49 \text{ mol\%Yb, 1 mol\%Tm}$  nanocrystals (Fig. 2d). Note that the integrated UV-to-NIR emission intensity ratio of 1.20 is also the highest among  $Tm^{3+}$ -activated core-only UC nanocrystals (Table S1†).

As shown in Fig. 3a and b, both  $\alpha-NaYF_4$  and  $Cs_2NaYF_6$  are face-centered cubic crystals with the space-group symmetry of  $Fm\bar{3}m$ . In  $\alpha-NaYF_4$  and  $Cs_2NaYF_6$ ,  $Ln^{3+}$  dopants like  $Yb^{3+}$  and  $Tm^{3+}$  ions are doped to substitute for  $Y^{3+}$  ions. The nearest distance between  $Yb^{3+}$  and  $Tm^{3+}$  ions is  $3.87 \text{ \AA}$  in  $\alpha-NaYF_4$  (Fig. 3a), which is much smaller relative to that in  $Cs_2NaYF_6$  ( $6.42 \text{ \AA}$ , Fig. 3b). As such, the excitation energy in  $\alpha-NaYF_4$  may be easily depleted owing to the increased probability of energy migration, which does not favor the multiphoton UCL emission.<sup>35</sup>

We investigated the microscopic models of  $Cs_2NaYF_6:Yb/Tm$  bulk materials and NPs (Fig. 3c). For each  $Tm^{3+}$  ion in bulk  $Cs_2NaYF_6:Yb/Tm$ , there are twelve nearest neighboring  $Ln^{3+}$  ions, four of which are situated at the top, middle or bottom [001] layer, respectively. The existence of isotropically substituted  $Ln^{3+}$  ions may promote the dissipation of the excitation energy in such a three-dimensional (3D) structured crystal sublattice.<sup>25,36,37</sup> By contrast, the  $Cs_2NaYF_6:Yb/Tm$  nanocrystalline materials experience an anisotropic growth

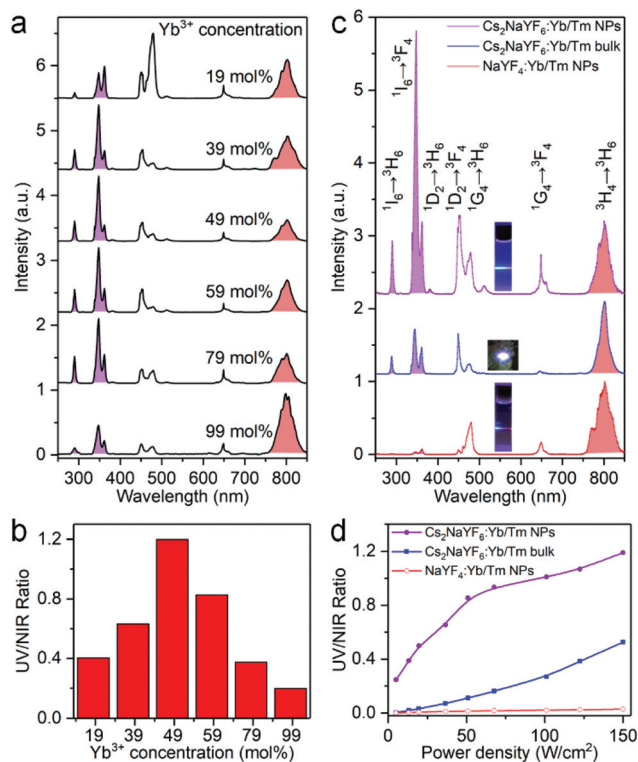


**Fig. 2** (a) UC emission spectra and (b) integrated UV-to-NIR emission intensity ratio of  $Cs_2NaYF_6:Yb/Tm$  NPs with different  $Yb^{3+}$  concentrations ( $\lambda_{ex} = 980 \text{ nm}$ , power density =  $150 \text{ W cm}^{-2}$ ). (c) UC emission spectra of  $Cs_2NaYF_6:49 \text{ mol\%Yb, 1 mol\%Tm}$  NPs, bulk and  $\alpha-NaYF_4:49 \text{ mol\%Yb, 1 mol\%Tm}$  NPs. These emission spectra were normalized at 803 nm of  $Tm^{3+}$  emission. Insets show their corresponding PL photographs. (d) Integrated UV-to-NIR emission intensity ratio in  $Cs_2NaYF_6:49 \text{ mol\%Yb, 1 mol\%Tm}$  NPs, bulk and  $\alpha-NaYF_4:49 \text{ mol\%Yb, 1 mol\%Tm}$  NPs upon 980 nm excitation with different power densities.

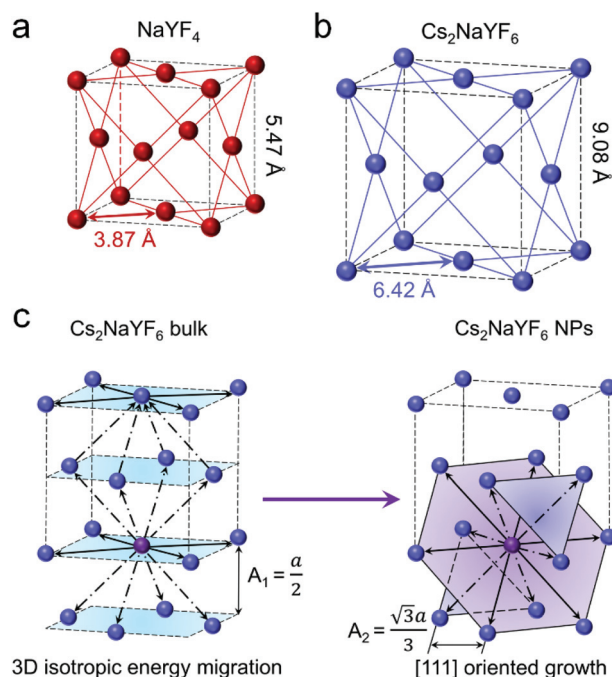


**Fig. 3** Schematic illustration of the structure of (a)  $\alpha-NaYF_4$  and (b)  $Cs_2NaYF_6:Yb/Tm$ , respectively. (c) Schematic illustration of the topological energy migration pathways in  $Cs_2NaYF_6:Yb/Tm$  bulk and NPs.

along the [111] orientation (Fig. 1g), resulting in two-dimensional (2D)-like nanoplatelets. For each  $\text{Tm}^{3+}$ , six nearest neighboring  $\text{Ln}^{3+}$  ions are situated at the middle [111] layer and the other six nearest neighboring  $\text{Ln}^{3+}$  ions are situated at the top and bottom [111] layer, respectively. Moreover, the distance between two [111] layers ( $A_2$ ) is calculated to be 5.24 Å, which is longer than that of two [100] layers ( $A_1$ , 4.54 Å).<sup>38</sup> Thus, such a 2D-like structure can effectively minimize the migration of excitation energy compared with the 3D structure,<sup>25,39</sup> which resulted in enhanced multiphoton UCL emission in  $\text{Cs}_2\text{NaYF}_6:\text{Yb}/\text{Tm}$  NPs relative to that in the bulk counterparts.

Besides  $\text{Tm}^{3+}$ , another  $\text{Ln}^{3+}$  ion like  $\text{Gd}^{3+}$  is often doped into inorganic nanocrystals to produce UV emission.<sup>40</sup> In this regard, we synthesized  $\text{Cs}_2\text{NaYF}_6:\text{Yb}/\text{Tm}/\text{Gd}$  NPs with different  $\text{Gd}^{3+}$  concentrations. EDX element mapping images indicate that the  $\text{Ln}^{3+}$  dopants are homogeneously distributed among the as-prepared NPs (Fig. S6†). Upon 980 nm excitation, a sharp UV emission peak at 311 nm can be observed, which originated from the  ${}^6\text{P}_{7/2} \rightarrow {}^8\text{S}_{7/2}$  transition of the  $\text{Gd}^{3+}$  ion (Fig. 4a). The luminescence intensity of such UV emission increased with increasing  $\text{Gd}^{3+}$  content from 10 mol% to 30 mol%, and then decreased at higher concentrations. Meanwhile, the five-photon  ${}^1\text{I}_6 \rightarrow {}^3\text{H}_6$  and  ${}^3\text{F}_4$  transitions of  $\text{Tm}^{3+}$  peaking at 290 and 348 nm continuously decreased with an increase in the  $\text{Gd}^{3+}$  concentrations. Moreover, in a control experiment by replacing  $\text{Cs}_2\text{NaYF}_6:\text{Yb}/\text{Tm}/\text{Gd}$  with  $\text{Cs}_2\text{NaYF}_6:\text{Yb}/\text{Gd}$  NPs under otherwise identical conditions, negligible UCL was detected, which indicates that the luminescence of  $\text{Gd}^{3+}$  was mainly sensitized by the nearby  $\text{Tm}^{3+}$  ions.

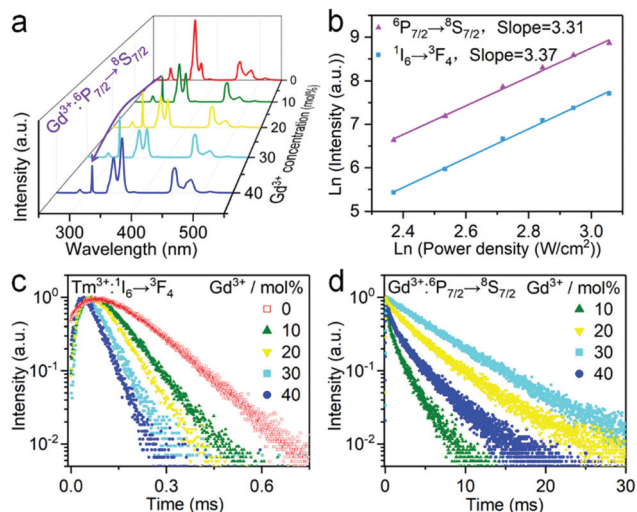


**Fig. 4** (a) UC emission spectra of  $\text{Cs}_2\text{NaYF}_6:\text{Yb}/\text{Tm}/\text{Gd}$  NPs with different  $\text{Gd}^{3+}$  contents. These spectra were normalized at 450 nm of  $\text{Tm}^{3+}$  emission. (b) Ln–Ln plots of the UC emission intensity versus excitation power density for the transitions of  ${}^6\text{P}_{7/2} \rightarrow {}^8\text{S}_{7/2}$  of  $\text{Gd}^{3+}$  and  ${}^1\text{I}_6 \rightarrow {}^3\text{F}_4$  of  $\text{Tm}^{3+}$  in  $\text{Cs}_2\text{NaYF}_6:\text{Yb}/\text{Tm}/\text{Gd}$  NPs, respectively. (c) PL decays of  ${}^1\text{I}_6 \rightarrow {}^3\text{F}_4$  of  $\text{Tm}^{3+}$  and (d)  ${}^6\text{P}_{7/2} \rightarrow {}^8\text{S}_{7/2}$  of  $\text{Gd}^{3+}$  in  $\text{Cs}_2\text{NaYF}_6:\text{Yb}/\text{Tm}/\text{Gd}$  NPs by monitoring the emissions at 348 nm and 311 nm, respectively.

To shed more light on the mechanism of the UV emission of  $\text{Gd}^{3+}$ , we obtained the UC spectra of  $\text{Cs}_2\text{NaYF}_6:\text{Yb}/\text{Tm}/\text{Gd}$  NPs excited with a 980 nm laser with different power densities. For a typical UC emission process, the value of pump photons ( $n$ ) required to populate a certain emission can be determined by the relationship of  $I \propto P^n$ , where  $I$  and  $P$  are the UCL intensity and the pump power density, respectively. The  $n$  value for  ${}^1\text{I}_6 \rightarrow {}^3\text{F}_4$  (348 nm) of  $\text{Tm}^{3+}$  was determined to be essentially identical to that of  ${}^6\text{P}_{7/2} \rightarrow {}^8\text{S}_{7/2}$  (311 nm) of  $\text{Gd}^{3+}$  (Fig. 4b), which indicates that the UCL of  $\text{Gd}^{3+}$  may occur through the sensitization of the  ${}^1\text{I}_6$  state of  $\text{Tm}^{3+}$ .

To further verify the process of energy transfer from  $\text{Tm}^{3+}$  to  $\text{Gd}^{3+}$ , we measured the UCL decays from  ${}^1\text{I}_6$  of  $\text{Tm}^{3+}$  and  ${}^6\text{P}_{7/2}$  of  $\text{Gd}^{3+}$  in  $\text{Cs}_2\text{NaYF}_6:\text{Yb}/\text{Tm}/\text{Gd}$  NPs. The effective lifetime of the  ${}^6\text{P}_{7/2}$  level of  $\text{Gd}^{3+}$  increased from 1.61 ms to 7.03 ms with increasing  $\text{Gd}^{3+}$  content from 10 mol% to 30 mol%, and then decreased to 2.97 ms at higher concentrations (Fig. 4c and Table S2†). Meanwhile, the effective lifetime of the  ${}^1\text{I}_6$  level of the  $\text{Tm}^{3+}$  ion was determined to be shortened from 163.96  $\mu\text{s}$  to 50.47  $\mu\text{s}$  with the increase of  $\text{Gd}^{3+}$  concentration from 0 to 40 mol% (Fig. 4d and Table S2†). All these results verified that the UCL of the  ${}^6\text{P}_{7/2}$  state of  $\text{Gd}^{3+}$  is sensitized by the  ${}^1\text{I}_6$  state of  $\text{Tm}^{3+}$  ions.

It has been reported that  $\text{Gd}^{3+}$  can be used as a bridge ion to sensitize a variety of  $\text{Ln}^{3+}$  ions (e.g.,  $\text{Eu}^{3+}$  or  $\text{Tb}^{3+}$ ) without long-lived intermediate energy states to produce UC emission.<sup>41,42</sup> For  $\text{Cs}_2\text{NaYF}_6:\text{Yb}/\text{Tm}/\text{Gd}/\text{Eu}$  and  $\text{Cs}_2\text{NaYF}_6:\text{Yb}/\text{Tm}/\text{Gd}/\text{Tb}$  NPs, a set of new UC emission peaks appeared besides those of  $\text{Tm}^{3+}$  and  $\text{Gd}^{3+}$  upon excitation at 980 nm (Fig. 5a). These newly appeared UC emission peaks can be assigned to the  ${}^5\text{D}_0 \rightarrow {}^7\text{F}_j$  transitions of  $\text{Eu}^{3+}$  and  ${}^5\text{D}_4 \rightarrow {}^7\text{F}_j$  transitions of  $\text{Tb}^{3+}$ , respectively. Correspondingly, the overall UC color output turned from blue to pink or cyan, respectively (insets of Fig. 5a).

The UC mechanism responsible for the intense UCL of  $\text{Eu}^{3+}$  and  $\text{Tb}^{3+}$  in  $\text{Cs}_2\text{NaYF}_6$  is illustrated in Fig. 5b. Upon excitation with a 980 nm laser, sensitizer ions ( $\text{Yb}^{3+}$ ) absorb the pumped photons, followed by energy transfer to the neighboring  $\text{Tm}^{3+}$  to populate the  ${}^3\text{F}_4$ ,  ${}^3\text{H}_4$ ,  ${}^1\text{G}_4$ ,  ${}^1\text{D}_2$ , and  ${}^1\text{I}_6$  states of  $\text{Tm}^{3+}$  in sequence. Note that the energy of the  ${}^6\text{P}_{7/2}$  level of the  $\text{Gd}^{3+}$  ion matches well with that of the  ${}^1\text{I}_6$  level of the  $\text{Tm}^{3+}$  ion. Once the  ${}^1\text{I}_6$  level of the  $\text{Tm}^{3+}$  ion is populated, its excitation energy will be partially transferred to the  $\text{Gd}^{3+}$  ion. The excitation energy will then be transferred to the  $\text{Eu}^{3+}$  or  $\text{Tb}^{3+}$  ion, because the  ${}^6\text{P}_{7/2}$  level of the  $\text{Gd}^{3+}$  ion matches well with the  ${}^5\text{H}_j$  level of  $\text{Eu}^{3+}$  or the  ${}^5\text{D}_j$  level of  $\text{Tb}^{3+}$ . As a result, red UCL of  $\text{Eu}^{3+}$  or green UCL of  $\text{Tb}^{3+}$  can be observed. The proposed energy transfer mechanism was further confirmed by the observed UCL decays. It was determined that the photoluminescence lifetime of  ${}^6\text{P}_{7/2}$  of  $\text{Gd}^{3+}$  was shortened from 7.03 ms to 2.83 ms, and the photoluminescence lifetime of  ${}^1\text{I}_6$  of  $\text{Tm}^{3+}$  was shortened from 59.89  $\mu\text{s}$  to 40.93  $\mu\text{s}$  after the doping of  $\text{Eu}^{3+}$  (Fig. S7†).

It is worth emphasizing that two key issues contribute to the generation of efficient UCL of  $\text{Eu}^{3+}$  and  $\text{Tb}^{3+}$  in  $\text{Cs}_2\text{NaYF}_6:\text{Yb}/\text{Tm}/\text{Gd}/\text{Eu}$  and  $\text{Cs}_2\text{NaYF}_6:\text{Yb}/\text{Tm}/\text{Gd}/\text{Tb}$  NPs, respectively.

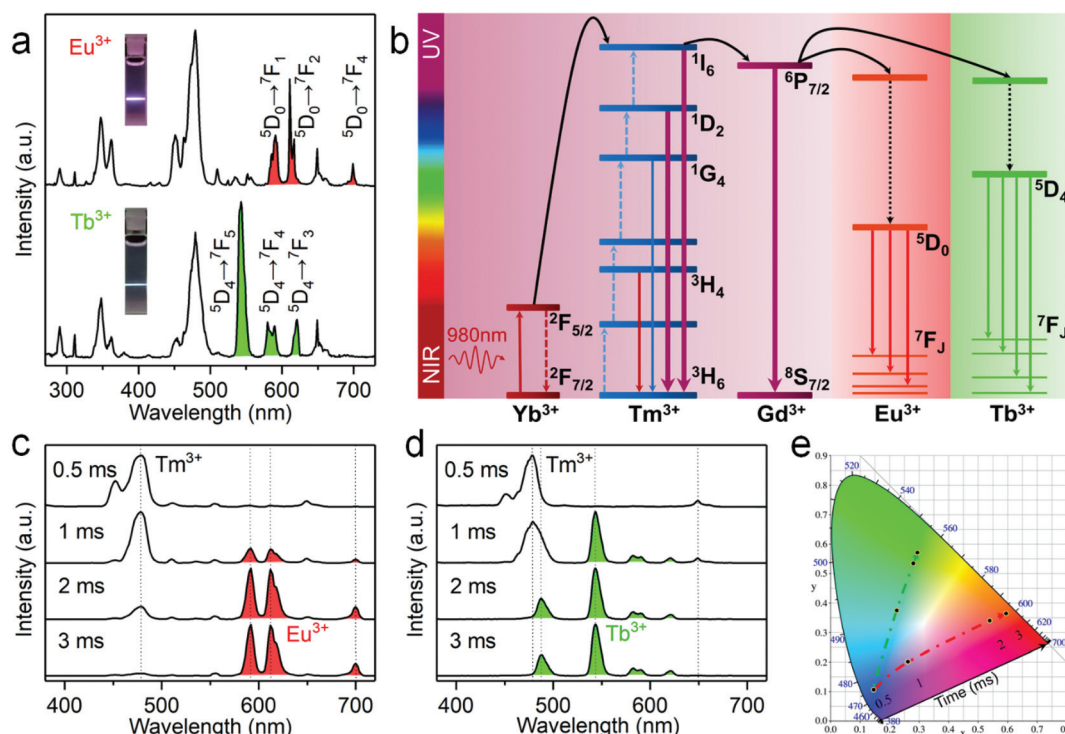


**Fig. 5** (a) UCL spectra of Cs<sub>2</sub>NaYF<sub>6</sub>:Yb/Tm/Gd/Eu and Cs<sub>2</sub>NaYF<sub>6</sub>:Yb/Tm/Gd/Tb NPs dispersed in hexane upon excitation at 980 nm with a power density of 150 W cm<sup>-2</sup>. Insets show their PL photographs. (b) Schematic energy level diagram showing the sensitization mechanism of Eu<sup>3+</sup> (red) and Tb<sup>3+</sup> (green) in Cs<sub>2</sub>NaYF<sub>6</sub>:Yb/Tm/Gd/Eu and Cs<sub>2</sub>NaYF<sub>6</sub>:Yb/Tm/Gd/Tb, respectively. The time evolution of UCL spectra for the (c) Cs<sub>2</sub>NaYF<sub>6</sub>:Yb/Tm/Gd/Eu and (d) Cs<sub>2</sub>NaYF<sub>6</sub>:Yb/Tm/Gd/Tb NPs upon excitation with a 980 nm pulse laser as the excitation source with the average power density of ~40 W cm<sup>-2</sup>. (e) Corresponding CIE chromaticity coordinates for Cs<sub>2</sub>NaYF<sub>6</sub>:Yb/Tm/Gd/Eu (red) and Cs<sub>2</sub>NaYF<sub>6</sub>:Yb/Tm/Gd/Tb (green) NPs in (c) and (d), respectively.

Firstly, Gd<sup>3+</sup> plays an important role as the energy transfer bridge. Without the doping of Gd<sup>3+</sup>, the UCL of Eu<sup>3+</sup> in Cs<sub>2</sub>NaYF<sub>6</sub>:Yb/Tm/Eu NPs was observed to be negligibly weak because of the large energy mismatch between the <sup>2</sup>F<sub>5/2</sub> → <sup>2</sup>F<sub>7/2</sub> transition of Yb<sup>3+</sup> and the <sup>5</sup>D<sub>J</sub> → <sup>7</sup>F<sub>J</sub> transition of Eu<sup>3+</sup>. As such, the UCL of Eu<sup>3+</sup> cannot be efficiently sensitized by the direct energy transfer between Tm<sup>3+</sup> and Eu<sup>3+</sup>. By contrast, additional doping of Gd<sup>3+</sup> resulted in much enhanced UCL of Eu<sup>3+</sup> by ~25 times (Fig. S8†). In addition, the confined energy migration of Ln<sup>3+</sup> dopants in the Cs<sub>2</sub>NaYF<sub>6</sub> lattice is also critical. Note that in the previous reports regarding the generation of UCL from Eu<sup>3+</sup> and Tb<sup>3+</sup>, the core-shell or core-multishell structure is a prerequisite for space separation of Tm<sup>3+</sup> and Eu<sup>3+</sup>/Tb<sup>3+</sup> so as to restrain the deleterious cross-relaxations between them.<sup>5,41</sup> In this work, the UCL of Eu<sup>3+</sup> in Cs<sub>2</sub>NaYF<sub>6</sub>:Yb/Tm/Gd/Eu NPs can be markedly enhanced by ~38 times that of traditional fluorides like α-NaYF<sub>4</sub>:Yb/Tm/Gd/Eu nanocrystals (Fig. S8†). To the best of our knowledge, such an efficient UCL of Eu<sup>3+</sup> or Tb<sup>3+</sup> in Cs<sub>2</sub>NaYF<sub>6</sub> NPs has not been realized in other Eu<sup>3+</sup> or Tb<sup>3+</sup>-doped core-only nanocrystals before.

As shown in Fig. 5a, the pure UCL of Eu<sup>3+</sup> or Tb<sup>3+</sup> cannot be obtained directly using the steady-state luminescence mode. The effective lifetimes of the <sup>5</sup>D<sub>0</sub> level of Eu<sup>3+</sup> and the <sup>5</sup>D<sub>4</sub> level of Tb<sup>3+</sup> in Cs<sub>2</sub>NaYF<sub>6</sub> NPs have been determined to be 2.60 ms and 2.25 ms, respectively (Fig. S9†), which are about two

orders of magnitude longer than those of Tm<sup>3+</sup> in these NPs (Fig. S7†). By virtue of the large difference in the UC luminescence lifetime between Eu<sup>3+</sup>/Tb<sup>3+</sup> and Tm<sup>3+</sup> ions, it is easy to separate their UCL based on the time-resolved detection technique by setting an appropriate delay time and gate time. Fig. 5c and d show the time-resolved UCL spectra of Cs<sub>2</sub>NaYF<sub>6</sub>:Yb/Tm/Gd/Eu and Cs<sub>2</sub>NaYF<sub>6</sub>:Yb/Tm/Gd/Tb NPs, respectively. Their UCL spectra were dominated by the emission of Tm<sup>3+</sup> when the delay time was within 1 ms. When the delay time is longer than 3 ms, pure red UCL attributed to the <sup>5</sup>D<sub>0</sub> → <sup>7</sup>F<sub>J</sub> (J = 1, 2, 3, and 4) transition of the Eu<sup>3+</sup> ion and green UCL attributed to the <sup>5</sup>D<sub>4</sub> → <sup>7</sup>F<sub>J</sub> (J = 3, 4, 5, and 6) transition of Tb<sup>3+</sup> were observed, respectively. As revealed by their corresponding CIE chromaticity coordinates (Fig. 5e), the UC color changed from blue to red or green for Cs<sub>2</sub>NaYF<sub>6</sub>:Yb/Tm/Gd/Eu or Cs<sub>2</sub>NaYF<sub>6</sub>:Yb/Tm/Gd/Tb NPs, respectively. Such an intriguing time-dependent UCL color output in Ln<sup>3+</sup>-doped Cs<sub>2</sub>NaYF<sub>6</sub> NPs is favorable for potential applications such as in time-resolved bioimaging and multilevel anti-counterfeiting.

## Conclusions

In summary, we have developed a new class of Ln<sup>3+</sup>-doped Cs<sub>2</sub>NaYF<sub>6</sub> NPs without a core/shell structure to achieve highly

efficient multiphoton UCL emissions. Upon excitation at 980 nm, intense UV emissions of  $\text{Tm}^{3+}$  were realized in  $\text{Cs}_2\text{NaYF}_6:\text{Yb}/\text{Tm}$  NPs by virtue of the large distance between the adjacent  $\text{Ln}^{3+}$  dopants in the host lattice. The optimal UV-to-NIR emission intensity ratio of  $\text{Cs}_2\text{NaYF}_6:\text{Yb}/\text{Tm}$  NPs has been determined to be 1.2, which is the highest among  $\text{Tm}^{3+}$ -activated core-only UC nanocrystals. Moreover, intense UV emission of  $\text{Gd}^{3+}$  has been realized in  $\text{Cs}_2\text{NaYF}_6:\text{Yb}/\text{Tm}/\text{Gd}^{3+}$  NPs via the energy transfer from  $\text{Tm}^{3+}$  to  $\text{Gd}^{3+}$ . Particularly, we have demonstrated that bright red and green UC emissions of  $\text{Eu}^{3+}$  and  $\text{Tb}^{3+}$  can be generated via the cascade sensitization of  $\text{Tm}^{3+}$  and  $\text{Gd}^{3+}$  in  $\text{Cs}_2\text{NaYF}_6:\text{Yb}/\text{Tm}/\text{Gd}/\text{Eu}$  and  $\text{Cs}_2\text{NaYF}_6:\text{Yb}/\text{Tm}/\text{Gd}/\text{Tb}$  NPs, respectively. These findings reveal the great potential of tuning UCL emissions in  $\text{Ln}^{3+}$ -doped  $\text{Cs}_2\text{NaYF}_6$  NPs, which may open up a promising avenue for the exploitation of  $\text{Ln}^{3+}$ -doped nanocrystals with excellent optical properties for versatile applications.

## Experimental

Detailed experimental procedures are reported in the ESI.†

## Author contributions

C. Z. prepared samples and collected data for the original draft. S.Y. H. and P. Z. assisted in PL measurements. L.P. W., S. H. Y., J. X. and R.F. L. contributed to conceptualization and investigation. C. Z., D.T. T. and X.Y. C. prepared the manuscript.

## Conflicts of interest

There are no conflicts to declare.

## Acknowledgements

This work was supported by the Science and Technology Cooperation Fund between Chinese and Australian Governments (2017YFE0132300), the Strategic Priority Research Program of the CAS (XDB20000000), the NSFC (no. U1805252, 21975257, 21771185, 12074380, and 11704380), and the CAS/SAFEA International Partnership Program for Creative Research Teams, NSF of Fujian Province (no. 2019I0029).

## Notes and references

- M. L. Deng, Y. X. Ma, S. Huang, G. F. Hu and L. Y. Wang, *Nano Res.*, 2011, **4**, 685–694.
- B. Zhou, B. Shi, D. Jin and X. Liu, *Nat. Nanotechnol.*, 2015, **10**, 924–936.
- D. Li, S. H. Yu and H. L. Jiang, *Adv. Mater.*, 2018, **30**, 1707377.
- W. J. Yao, Q. Y. Tian, B. Tian, M. X. Li, H. J. Wang, P. Zeng, L. Liu, H. Zheng and W. Wu, *Sci. China Mater.*, 2019, **62**, 368–378.
- M. Ding, B. Dong, Y. Lu, X. Yang, Y. Yuan, W. Bai, S. Wu, Z. Ji, C. Lu and K. Zhang, *Adv. Mater.*, 2020, **32**, 2002121.
- N. Xin, D. Wei, Y. Zhu, M. Yang, S. Ramakrishna, O. Lee, H. Luo and H. Fan, *Mater. Today Chem.*, 2020, **17**, 100329.
- J. K. Chen, S. X. Wang, J. D. Lin and D. Q. Chen, *Nanoscale*, 2019, **11**, 22359–22368.
- H. Huang, J. K. Chen, Y. T. Liu, J. D. Lin, S. X. Wang, F. Huang and D. Q. Chen, *Small*, 2020, **16**, 12.
- F. Wang, Y. Han, C. S. Lim, Y. Lu, J. Wang, J. Xu, H. Chen, C. Zhang, M. Hong and X. Liu, *Nature*, 2010, **463**, 1061–1065.
- C. Zhang, L. D. Sun, Y. W. Zhang and C. H. Yan, *J. Rare Earths*, 2010, **28**, 807–819.
- S. Gai, C. Li, P. Yang and J. Lin, *Chem. Rev.*, 2014, **114**, 2343–2389.
- W. Luo, Y. Liu and X. Chen, *Sci. China Mater.*, 2015, **58**, 819–850.
- X. W. Zhang, Z. Zhao, X. Zhang, D. B. Cordes, B. Weeks, B. S. Qiu, K. Madanan, D. Sardar and J. Chaudhuri, *Nano Res.*, 2015, **8**, 636–648.
- Q. Zou, P. Huang, W. Zheng, W. You, R. Li, D. Tu, J. Xu and X. Chen, *Nanoscale*, 2017, **9**, 6521–6528.
- J. Shen, G. Chen, T. Y. Ohulchanskyy, S. J. Kesseli, S. Buchholz, Z. Li, P. N. Prasad and G. Han, *Small*, 2013, **9**, 3213–3217.
- A. Punjabi, X. Wu, A. Tokatli-Apollon, M. El-Rifai, H. Lee, Y. Zhang, C. Wang, Z. Liu, E. M. Chan and C. Duan, *ACS Nano*, 2014, **8**, 10621–10630.
- S. Wen, J. Zhou, K. Zheng, A. Bednarkiewicz, X. Liu and D. Jin, *Nat. Commun.*, 2018, **9**, 2415.
- B. Chen and F. Wang, *Acc. Chem. Res.*, 2019, **53**, 358–367.
- L. Tu, X. Liu, F. Wu and H. Zhang, *Chem. Soc. Rev.*, 2015, **44**, 1331–1345.
- L. Zhao, J. Peng, Q. Huang, C. Li, M. Chen, Y. Sun, Q. Lin, L. Zhu and F. Li, *Adv. Funct. Mater.*, 2014, **24**, 363–371.
- Q. S. Chen, X. J. Xie, B. L. Huang, L. L. Liang, S. Y. Han, Z. G. Yi, Y. Wang, Y. Li, D. Y. Fan, L. Huang and X. G. Liu, *Angew. Chem., Int. Ed.*, 2017, **56**, 7605–7609.
- S. Mei, J. Zhou, H. T. Sun, Y. Cai, L. D. Sun, D. Jin and C. H. Yan, *Adv. Sci.*, 2021, 2003325.
- B. Zhou, B. Tang, C. Zhang, C. Y. Qin, Z. J. Gu, Y. Ma, T. Y. Zhai and J. N. Yao, *Nat. Commun.*, 2020, **11**, 1174.
- X. Chen, L. M. Jin, W. Kong, T. Y. Sun, W. F. Zhang, X. H. Liu, J. Fan, S. F. Yu and F. Wang, *Nat. Commun.*, 2016, **7**, 10304.
- J. Wang, R. Deng, M. A. MacDonald, B. Chen, J. Yuan, F. Wang, D. Chi, T. S. A. Hor, P. Zhang and G. Liu, *Nat. Mater.*, 2014, **13**, 157–162.
- L. Marciniak, W. Strek, A. Bednarkiewicz, A. Lukowiak and D. Hreniak, *Opt. Mater.*, 2011, **33**, 1492–1494.
- T. Pawlik and J. M. Spaeth, *J. Appl. Phys.*, 1997, **82**, 4236–4240.

- 28 V. N. Makhov, N. M. Khaidukov, D. Lo, J. C. Krupa, M. Kirm and E. Negodin, *Opt. Mater.*, 2005, **27**, 1131–1137.
- 29 P. A. Loiko, N. M. Khaidukov, J. Mendez-Ramos, E. V. Vilejshikova, N. A. Skoptsov and K. V. Yumashev, *J. Lumin.*, 2016, **175**, 260–266.
- 30 P. A. Loiko, E. V. Vilejshikova, N. M. Khaidukov, J. Mendez-Ramos, X. Mateos and K. V. Yumashev, *J. Lumin.*, 2017, **185**, 279–285.
- 31 P. A. Tanner, Y. L. Liu, N. M. Edelstein, K. M. Murdoch and N. M. Khaidukov, *J. Phys.: Condens. Matter*, 1997, **9**, 7817–7836.
- 32 Y. M. Yang, Z. Y. Li, J. Y. Zhang, Y. Lu, S. Q. Guo, Q. Zhao, X. Wang, Z. J. Yong, H. Li, J. P. Ma, Y. Kuroiwa, C. Moriyoshi, L. L. Hu, L. Y. Zhang, L. R. Zheng and H. T. Sun, *Light: Sci. Appl.*, 2018, **7**, 11.
- 33 J. Gu, Z. Q. Zhao, Y. Ding, H. L. Chen, Y. W. Zhang and C. H. Yan, *J. Am. Chem. Soc.*, 2013, **135**, 8363–8371.
- 34 W. Lee, D. Choi and S. Kim, *Chem. Mater.*, 2020, **32**, 6864–6874.
- 35 O. Malta, *J. Non-Cryst. Solids*, 2008, **354**, 4770–4776.
- 36 H.-X. Mai, Y.-W. Zhang, R. Si, Z.-G. Yan, L.-d. Sun, L.-P. You and C.-H. Yan, *J. Am. Chem. Soc.*, 2006, **128**, 6426–6436.
- 37 G. Wang, Q. Peng and Y. Li, *J. Am. Chem. Soc.*, 2009, **131**, 14200–14201.
- 38 K. Momma and F. Izumi, *J. Appl. Crystallogr.*, 2011, **44**, 1272–1276.
- 39 T. C. Ozawa, K. Fukuda, K. Akatsuka, Y. Ebina and T. Sasaki, *Chem. Mater.*, 2007, **19**, 6575–6580.
- 40 V. Mahalingam, R. Naccache, F. Vetrone and J. A. Capobianco, *Chem. – Eur. J.*, 2009, **15**, 9660–9663.
- 41 F. Wang, R. Deng, J. Wang, Q. Wang, Y. Han, H. Zhu, X. Chen and X. Liu, *Nat. Mater.*, 2011, **10**, 968–973.
- 42 X. Chen, D. Peng, Q. Ju and F. Wang, *Chem. Soc. Rev.*, 2015, **44**, 1318–1330.